Acta Pharmaceutica Sinica B 2025;15(2):1084−1097

Chinese Pharmaceutical Association
Institute of Materia Medica, Chinese Academy of Medical Sciences

Acta Pharmaceutica Sinica B

www.elsevier.com/locate/apsb
www.sciencedirect.com

ORIGINAL ARTICLE

Locally producing antibacterial peptide to deplete intratumoral pathogen for preventing metastatic breast cancer

Shizhen Geng[a,b,†], Tingting Xiang[b,†], Yaru Shi[b], Mengnian Cao[b], Danyu Wang[b], Jing Wang[b], Xinling Li[b], Haiwei Song[b], Zhenzhong Zhang[b], Jinjin Shi[b], Junjie Liu[b], Airong Li[b,*], Ke Sun[a,*]

[a]*Department of Urinary Surgery, the First Affiliated Hospital of Zhengzhou University, Zhengzhou 450052, China*
[b]*School of Pharmaceutical Sciences, Zhengzhou University, Zhengzhou 450001, China*

Received 26 September 2024; received in revised form 30 November 2024; accepted 18 December 2024

KEY WORDS

Intratumoral pathogen;
Metastasis;
Antibacterial peptide;
Optogenetics;
Breast cancer;
Fusobacterium nucleatum;
Cancer-associated fibroblast;
Mild heat

Abstract Metastatic dissemination is the major cause of death from breast-cancer (BC). *Fusobacterium nucleatum* (*F.n*) is widely enriched in BC and has recently been identified as one of the high-risk factors for promoting BC metastasis. Here, with an experimental model, we demonstrated that intratumoral *F.n* induced BC aggressiveness by transcriptionally activating Epithelial-mesenchymal transition-associated genes. Therefore, the *F.n* may be a potential target to prevent metastasis. Given the fact that cancer-associated fibroblasts (CAFs) are abundant in BC and located near blood vessels, we report an optogenetic system that drives CAF to *in situ* produce human antibacterial peptide LL37, with the characteristics of biosafety and freely intercellular trafficking, for depleting intratumoral *F.n*, leading to a 72.1% reduction in lung metastatic nodules number without affecting the balance of the systemic flora. Notably, mild photothermal treatment was found that could normalize CAF, contributing to synergistically inhibiting BC metastasis. In addition, the system can also simultaneously encode a gene of TNF-related apoptosis-inducing ligand to suppress the primary tumor. Together, our study highlights the potential of local elimination of tumor pathogenic bacteria to prevent BC metastasis.

*Corresponding authors.
E-mail addresses: liairong@zzu.edu.cn (Airong Li), fccsunk1@zzu.edu.cn (Ke Sun).
[†]These authors made equal contributions to this work.

Peer review under the responsibility of Chinese Pharmaceutical Association and Institute of Materia Medica, Chinese Academy of Medical Sciences.

https://doi.org/10.1016/j.apsb.2025.01.002

1. Introduction

Metastatic breast-cancer (MBC) is a leading cause of cancer-related female mortality worldwide[1,2], and despite improvements in BC treatments, the 5-year survival rate of MBC patients remains low at only 30%[3]. Therefore, it is crucial to elucidate the underlying mechanisms of metastasis in MBC patients. Recently, the intratumoral microbiota has been identified as an integral tumor component[4-6], and microbiota−host interactions play an important role in the progression of BC[7-10]. With the development of metagenomics sequencing, descriptive analysis of the breast tumor microbiota gained explosive growth, and a variety of microbiota involved in BC carcinogenesis have been revealed, such as *Fusobacterium nucleatum* (*F.n*)[11], *Archangium*[12] and *Dicipivirus*[13]. The research found that the lectin Fap2 mediated the recognition of host Gal-GalNAc by *F.n* and helped *F.n* to localize in BC tissues abundantly[14]. Notably, clinical data showed that *F.n* increased abundance in higher-stage BC and is highly associated with metastasis. However, the mechanism for *F.n* in BC metastasis has not yet been fully elucidated.

In an experimental model, we observed that *F.n* significantly promoted lung metastasis of BC and revealed that intratumoral *F.n* induced BC aggressiveness by activating Epithelial-mesenchymal transition (EMT) that largely determines the invasion/spread and subsequent re-localization of cancer cells in distant organs[15-16]. Therefore, destroying intratumoral *F.n* is a potential therapeutic strategy for anti-BC metastasis. Compared with traditional antibiotics, antimicrobial peptides have obvious advantages in directly killing pathogens without inducing drug resistance[17-18]. In particular, the human antimicrobial peptide LL37, an intrinsic part of the human innate immune system[19], can move freely across the cell membrane and between cells[20] with low toxicity to the host cells[21], which has been successfully applied in human clinical studies[22-23]. However, systematically administrated LL37 has poor physicochemical stability[24-25] and a high risk of disrupting the balance of the systemic microflora. Recently, optogenetics has been adopted for accurately regulating the expression of polypeptides or proteins[26-27], with the advantage of noninvasiveness, spatial specificity and reversibility[28]. Thus, *in situ* expression of LL37 by the optogenetic system has the potential for local elimination of *F.n* with high precision and spatial specificity.

Given the fact that CAF preferentially captures most of the nanoparticles or drugs attempting to enter the tumor core site because they are always located near blood vessels and are abundant in BC[29-30], an optogenetic system (OBA/pHSP-LL37) targeting CAF was designed, composed of the eutectic mixture (ONP), aminoethyl anisamide-grafted albumin and LL37 plasmid, which drives CAF to *in situ* produce human antibacterial peptide LL37 for depleting intratumoral *F.n* without affecting the balance of the systemic flora (Scheme 1). Notably, the ONP has excellent reversible thermochromism, which supports the optogenetic system to maintain a preset temperature (42 °C) under laser irradiation to avoid damage to transfected cells caused by hyperthermia. Unexpectedly, CAF morphology was altered upon exposure to mild heat, and the transcriptome results revealed that CAF was quiesced, which will contribute to synergistic inhibition of BC metastasis. Besides, we added a TNF-related apoptosis-inducing ligand (TRAIL) to the plasmid in the optogenetic system (referred to as OBA/pHSP-LL37-TRAIL) to suppress primary tumor and metastasis. Together, the strategy of depleting intratumoral pathogenic microorganisms provides a new perspective for preventing BC metastasis.

2. Materials and methods

2.1. Materials

2-Anilino-6-(dibutylamino)-3-methylfluoran (ODB-2), polyethylene glycol (PEG), and taipan blue staining cell viability assay kits were purchased from Shanghai Yuanye (China). β-Naphthol (Naph) and ethylamine were purchased from Sinopharm (China). DNase I, bovine serum albumin (BSA), paclitaxel (PTX), DMEM and RPMI1640 were purchased from Beijing Solaibao (China). Fetal bovine serum was purchased from Gibco (USA). A rapid plasmid extraction kit was purchased from Novozymes (China).

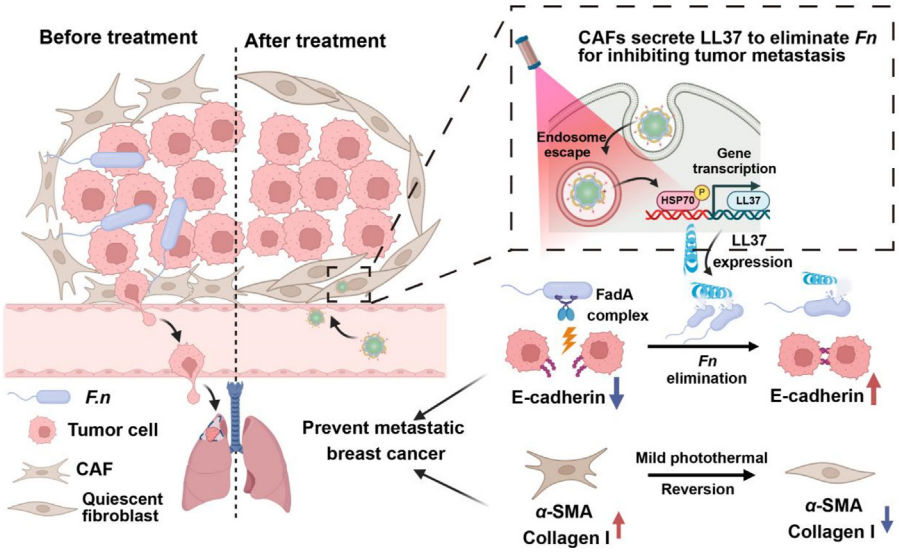

Scheme 1 Schematic diagram of the optogenetic system locally producing antibacterial peptide to deplete intratumoral pathogen for preventing metastatic BC.

Lysosomal green fluorescent probes were purchased from Thermo Fisher Scientific (USA). Annexin V-FITC Apoptosis Detection Kit was purchased from KEYGEN BIOTECH (China).

2.2. Cell lines and bacterial strains

Mouse breast cancer cell line (4T1) was obtained from Targeting Therapy and Diagnosis for Critical Diseases, Henan Province, China. Mouse embryonic fibroblasts (NIH3T3) were obtained from Procell Life Science&Technology (China). The cell lines were cultured in RPMI1640 or DMEM (Gibco, USA) containing 10% FBS (Gibco, USA) (5% CO_2, 37 °C).

F. nucleatum (*F.n*, ATCC 25586) was purchased from the Shanghai Strain Conservation Center (China), and cultured at 37 °C in an anaerobic environment (10% CO_2, 10% H_2, 80% N_2). Fresh medium of *F.n* was prepared with Brain Heart Infusion broth (BHI, Guangdong Huankai Microbial Sci. & Tech, China). All bacteria were purified from colonies isolated on the plates for subsequent liquid pass-aging cultures. The optical density (OD) values of the bacterial suspensions were measured using UV absorption spectrometry (Shimadzu, Japan) at 600 nm (OD_{600} of 0.1 corresponds to 1×10^8 CFU/mL).

2.3. Evaluating the effect of different temperatures on cell viability

NIH3T3 was induced to CAF with 10 ng/μL TGF-β (PeproTech, China). CAF was inoculated into 96-well plates at 8×10^3/well density and heated at different temperatures for 30 min (37, 39, 42, and 45 °C) after growth density to 90%. Absorbance at 450 nm was measured on a microplate absorbance reader (Thermo Science, USA) to calculate cell viability.

2.4. Construction of pHSP-LL37 and pHSP-LL37-TRAIL

Plasmid pHSP-LL37 contains a heat promoter (HSP70 promoter) and *F.n* targeting LL37 (this part is a fusion protein containing *F.n* targeting peptide EC5, antimicrobial peptide LL37). Besides the HSP70 promoter and LL37, the apoptosis protein TRAIL was added to pHSP-LL37-TRAIL. The plasmids were synthesized by the Shenzhen Genomics Institute (China).

2.5. Preparation and characterization of OBA

To synthesize cBSA, BSA (20 mg) was dissolved in 5 mL of deionized water. Then, the solution above was mixed with 5 mL of 1 mol/L ethylamine and the pH was adjusted to 4.75 with hydrochloric acid. After 20 min, the appropriate amount of EDC and NHS were added (EDC:NHS molar ratio of 4:5), and the mixture was stirred slowly at room temperature for 2 h. The reaction was terminated by adding 110 μL of 4 mol/L acetic acid-sodium acetate (pH = 4.75). The samples were dialyzed with 8000–14,000 Da dialysis bags for 48 h and then were freeze-dried for 2 days. After that, cBSA was obtained and characterized by Infrared spectroscopy analysis (FT-IR) (Thermo Fisher Scientific, USA) and Dynamic light scattering (DLS).

Subsequently, the cBSA was modified with the targeting ligand aminoethyl anisamide (AEAA) by amide reaction. In brief, appropriate amounts of EDC and NHS were added to the AEAA-PEG-COOH solution (1 mg/mL) and the mixture was stirred slowly at room temperature for 15 min. The pH of the solution was raised to 7.2−7.5, and the cBSA solution was added and stirred at room temperature for 2 h. The solution was collected and dialyzed using deionized water for 48 h (MWCO = 8000–14,000 Da) and freeze-dried to obtain cBSA-A. cBSA-A was characterized by FT-IR.

Finally, the reversible thermochromic nanoparticles ONP@cBSA-A (OBA) were prepared by dispersing the molten ONP into cBSA-A. In brief, a mixture of ODB-2:Naph:PEG = 1:5:60 was heated to a molten state by an infrared heater, and the obtained ONP was dissolved in acetone, and then added to the cBSA-A solution. The above mixture was stirred slowly overnight to form OBA. The melting points of ODB-2, Naph, PEG, and ONP samples were tested by differential scanning calorimetry (DSC) (NETZSCH, Germany).

2.6. Preparation and characterization of OBA/pDNA

The plasmid (pDNA) and OBA solution were diluted with DNase/RNase-free ddH_2O and stabilized in 1.5 mL EP tubes at room temperature for 5 min. Then, the two tubes were mixed according to the optimal weight ratio of pDNA and OBA, and stood at room temperature for 30 min to obtain OBA/pDNA. OBA/pDNA was characterized by DLS and Transmission electron microscope (TEM) (Hitachi HT7700, Japan).

2.7. Evaluation of photothermal performance in vitro

OBA was synthesized with different molecular weight PEGs (PEG1k, PEG2k, and PEG4k) and was exposed to laser irradiation at 660 nm (1.5 W/cm^2) for 30 min. The temperature of the OBA solution was measured with an infrared camera (FLuke, USA) to confirm the composition of the final formulation.

The precise temperature control capability of OBA was evaluated by varying the power density of the laser irradiation (1, 1.5, 2, and 2.5 W/cm^2), the concentration of OBA (30, 40, and 80 μg/mL) and initial temperature of OBA solution (20, 25, and 37 °C) under 660 nm laser irradiation.

The colour and UV absorption spectrum of the OBA solution (40 μg/mL) were observed and recorded before and after laser irradiation by an infrared camera (USA), and the temperature curves were plotted to estimate the reversible thermochromism of OBA.

OBA solution (40 μg/mL) was heated and cooled for five cycles to investigate the photothermal stability of OBA (660 nm, 1.5 W/cm^2).

2.8. Gel retardation assay

The pHSP-LL37 condensation ability of OBA was determined by agarose gel retardation assay. In brief, the OBA solution was mixed with pHSP-LL37 at different mass ratios (pHSP-LL37 amount of 500 ng). The mixture was gently vortexed for 30 s and allowed to stand at room temperature for 30 min. 1% Agarose gel electrophoresis was performed in 1 × TAE flow buffer and imaged using a gel imaging system (Syngene, USA).

To examine the ability of OBA to protect the plasmid, nuclease (DNase I) was co-incubated with OBA/pHSP-LL37. In brief, 1 μL of DNase I (2 U/μL) was added to OBA/pHSP-LL37 (containing 500 ng of pHSP-LL37) for 30 min at 37 °C. After that, 1 μL EDTA (100 mmol/L) was immediately added to terminate the reaction and agarose gel electrophoresis was performed.

2.9. Cytotoxicity assay in vitro

CAFs were inoculated into 96-well plates at a density of 8×10^3/well, and different concentrations of OBA/pHSP-LL37 (10, 20, 30, 40, 50, 60, and 80 μg/mL) were added after cell growth density reached 80%. The preparations were eluted with PBS after 24 h incubation and cell viability was determined by the CCK-8 method.

2.10. Cellular internalization assay

The CAF uptake of OBA/pDNA was observed by a Confocal Laser Scanning Microscope (CLSM) (Leica, Germany). CAFs were inoculated at a density of 8×10^4/well in a 24-well plate and cultured overnight. The free pDNA (labeled with Cy5), the OB/pDNA (without targeting ligand), and OBA/pDNA (with targeting ligand) were added into CAFs, respectively. After 4 h incubation at 37 °C, cell uptake was observed by CLSM.

2.11. Endosomal escape assay

CAFs were inoculated in 15 mm confocal dishes (1×10^5/dish) and cultured overnight. After transfection with OBA/pDNA (pDNA, 2.5 μg/dish, labeled with Cy5) for 1, 3, and 6 h, lysosomal escape was observed with CLSM.

2.12. Optogenetic activation assay in vitro

The green fluorescent protein (GFP) gene was encoded into the plasmid to investigate the optimal transfection conditions of OBA/pHSP-LL37. CAFs were inoculated at 8×10^4/well in 24-well plates and incubated for 24 h. After 6 h of OBA/pHSP-LL37 transfection, the supernatant was discarded and the wells were continuously exposed to laser (660 nm, 1.5 W/cm^2) for 15, 30, and 45 min, respectively. The expression of GFP in CAF was detected by CLSM and flow cytometry at 24 h to assess the optimal time point for laser irradiation.

The expression of GFP was detected by flow cytometry and CLSM to explore the optimal time for protein expression. After transfection with OBA/pHSP-LL37 (2 μg/well) for 6 h, the well plates were continuously exposed to laser (660 nm, 1.5 W/cm^2) for 30 min. The above cells were detected by CLSM and flow cytometry at 12, 24, and 48 h, respectively.

Based on the above analysis, expression of LL37 and TRAIL were investigated in mRNA and protein levels. CAFs were inoculated at 2×10^5/well in 6-well plates containing fresh medium with 10% FBS and incubated to 80% density. CAFs were treated with different preparations, respectively. Cells were collected to detect the mRNA expression of LL37 and TRAIL at 12 h post-laser irradiation. Under the same conditions, the supernatant of the above cell was collected at 24 h post-laser irradiation, and the levels of secreted proteins were quantified by enzyme-linked immunosorbent assay (ELISA).

2.13. Antibacterial experiments in vitro

The CAF was treated with control, OBA(−), OBA(+), OBA/pHSP-LL37(−), and OBA/pHSP-LL37(+), respectively. After that, the supernatant of CAF was collected and incubated with the *F.n* solution for 8 h at 37 °C. *F.n* was collected and resuspended with the configured PI staining working solution for 15 min. The killing of *F.n* was examined by flow cytometry and CLSM. In addition, *F.n* (1×10^5 CFU/mL) was co-incubated with supernatants from each group in 96-well plates for 24 h. UV absorbance was measured at 600 nm to monitor *F.n* growth during incubation.

To further estimate the antibacterial activity of OBA/pHSP-LL37, *F.n* (1×10^5 CFU/mL) was co-incubated with supernatants from each group at 37 °C for 8 h and the integrity of *F.n* was observed by Scanning electron microscopy (SEM) (Hitachi, Japan).

2.14. Tumor cell apoptosis assay

4T1 cells were inoculated into 6-well plates at a density of 2×10^5/well and cultured overnight. The supernatants of CAFs receiving different treatments were co-cultured with 4T1 for 24 h. After that, 4T1 cells were stained with Annexin V-FITC and PI, and detected by flow cytometry.

2.15. Animal care and use

BALB/c and BALB/c-nude mice (female, 6−8 weeks old) were purchased from SPF (Beijing) Biotechnology Co., Ltd. (China) and housed at Zhengzhou University Laboratory Animal Center at 25 °C and 55% humidity. The experimental animal license numbers are SCXK (Beijing) 2019-0010 and SCXK (Beijing) 2024-0001, respectively. Animals were bred following the Zhengzhou University Guide for the Care and Use of Laboratory Animals. All animal handling procedures were performed in accordance with the guidelines of the Regional Ethics Committee for Animal Experiments and the Care Regulations approved by the Institutional Animal Care and Use Committee of Zhengzhou University.

2.16. Animal model establishment

A *F.n*-infected fibrosis-metastatic breast cancer model was established to evaluate the anti-metastatic activity of OBA/pHSP-LL37(+). In brief, 4T1 cells (1×10^6 cells) and CAFs (5×10^5 cells) were co-inoculated into the right 3rd mammary fat pad of BALB/c mice. When the tumor size reached 400−500 mm^3, *F.n* (100 μL, 1×10^8 CFU) was given by intratumoral multi-point injections to establish *F.n*-infected breast cancer model.

2.17. Biodistribution analysis of OBA/pHSP-LL37

OB/pHSP-LL37 and OBA/pHSP-LL37 were labeled with Near-infrared fluorescent dye (IR783). The tumor-bearing mice were injected intravenously (i.v.) with IR783, OB/pHSP-LL37/IR783 and OBA/pHSP-LL37/IR783 (2 mg/kg of IR783), respectively. Live imaging was performed at predetermined time intervals (6, 12, 24, 48, and 72 h) after injection. Mice were executed at 72 h, and then the heart, liver, spleen, lung, kidney, and tumor were taken for *in vitro* fluorescence imaging.

2.18. Evaluation of photothermal performance in vivo

The tumor-bearing mice were injected i.v. with 120 μL PBS and OBA/pHSP-LL37 (24 μg plasmid per mouse), respectively. After 12 h of injection, the tumors' positions were exposed to a 660 nm laser for 30 min. The temperatures of the tumor sites were recorded with an infrared camera (USA). Morphological characteristics of the tumor sites were recorded with a camera before and after laser irradiation.

2.19. The anti-metastatic activity of the optogenetic system

The 4T1 tumor-bearing mice were randomly divided into 5 groups: control, OBA(−), OBA(+), OBA/pHSP-LL37(−), and OBA/pHSP-LL37(+) (120 μL, 24 μg plasmid per mouse, $n = 5$). "(+)" represents laser irradiation of mouse tumor tissue for 30 min (660 nm, 1.5 W/cm^2) at 12 h post-injection. The drug was administered i.v. at two-day intervals for a total of five doses. At the end of treatment, lungs and tumor tissues were gained. Metastasis nudes and sections of the lungs were observed to evaluate the anti-metastasis effect. Tumor tissues were stained to analyze intratumoral *F.n*, α-SMA, Masson staining, fibronectin, E-cadherin, and β-catenin, respectively.

2.20. The anti-metastatic activity of the LL37

The tumor-bearing nude mice were randomly divided into 2 groups: control, LL37 (100 μL, 3 μg per mouse, $n = 3$). The LL37 was administered intratumorally at two-day intervals for a total of five doses. At the end of treatment, lungs and tumor tissues were gained. Metastasis nudes of the lungs were observed to evaluate the anti-metastasis effect. Tumor tissues were stained to analyze intratumoral *F.n*.

2.21. Toxicity studies

Peripheral blood of 4T1 tumor-bearing mice was collected after single or multiple dosing to assess the biosafety of OBA/pHSP-LL37 (routine blood indicators: hemoglobin (HGB), mean red blood cell volume (MCV), platelets (PLT), and red blood cells (RBC); Indicators of liver function tests: total bilirubin (TBIL), alanine aminotransferase (ALT), aspartate aminotransferase (AST), and gamma-glutamyl transpeptidase (GGT); Indicators of renal function tests: creatinine (CREA), uric acid (UA), urea (UREA). Major organs were collected from 4T1 tumor-bearing mice and H&E staining was performed to further assess the biosafety of OBA/pHSP-LL37. Fecal specimens were collected for 16S rDNA sequencing to assess the effect of OBA/pHSP-LL37 on the gut microbiota.

2.22. The anticancer activity of the photoactivatable OBA/pHSP-LL37-TRAIL system

The tumor-bearing mice were randomly divided into 6 groups: (1) Control, (2) PTX, (3) OBA(+) + PTX, (4) OBA/pHSP-LL37(−) + PTX, (5) OBA/pHSP-LL37(+) + PTX, and (6) OBA/pHSP-LL37-TRAIL(+) ($n = 5$). The drugs were administered at two-day intervals for a total of five doses. After formulation injection, PTX (2 mg/kg) was administered by i.v. injection. The body weight and tumor size of mice were measured for a total of 18 days. Lungs were dissected to observe lung metastasis. Tumors were harvested for Fluorescence *in situ* hybridization (FISH) (*F.n*), immunohistochemistry (TRAIL, Ki67), and TUNEL staining.

2.23. Statistical analysis

Quantitative data were expressed as "mean ± standard deviation". One-way analysis of variance (ANOVA) and post hoc multiple comparison tests were used for comparisons between multiple groups, and independent samples *t*-tests were used for comparisons between two groups, plotted using SPSS. Differences were considered significant when $^*P < 0.05$, $^{**}P < 0.01$, $^{***}P < 0.001$, and $^{****}P < 0.0001$.

3. Results and discussion

3.1. F.n promotes BC metastasis by activating EMT signaling pathways

To investigate the effect of *F.n* on metastasis of BC, we constructed a 4T1 tumor-bearing mice model. On the 18th day after intratumoral multipoint injection of *F.n*, the lungs (one of the main metastatic organs of BC) were dissected and examined (without the *F.n* group, labeled as control; *F.n*-treated group, labeled as *F.n*). As shown in Supporting Information, Fig. S1A and S1B the lung metastatic nodule number in *F.n* group was significantly higher than that of the control group, suggesting that *F.n* promotes BC metastasis. We next seek to understand how *F.n* contributes to cancer cell invasiveness by transcriptional analyses of *F.n*-treated 4T1 tumor tissues. A total of 365 differentially expressed gene profiles were detected. Among these genes, 252 genes were up-regulated and 113 genes were down-regulated (Fig. S1C). Based on these differential genes, KEGG pathway enrichment analysis showed that *F.n* impacted multiple aspects of BC cells and nearly all these genes were involved in EMT, including Wnt signaling pathway, NF-Kappa B signaling pathway, IL-17 signaling pathway, focal adhesion, adhesion junction, tight junction and cell adhesion molecules, etc (Fig. S1D). In substantiating these changes, increased β-catenin (key EMT-related transcriptional factor cluster)[31] and reduced E-cadherin (loss of E-cadherin expression is a hallmark of EMT)[32] were verified at the protein level in the *F.n*-treated orthotopic tumors (Fig. S1E). Furthermore, the same trend was observed at the cellular level (Fig. S1F). The results demonstrated that *F.n* drives the transcriptional activation of the genes responsible for EMT induction. Given that EMT is the important driving force for cancer metastasis[33] and is highly associated with *F.n* in BC, depleting intratumoral *F.n* is a potential therapeutic strategy for anti-BC metastasis.

3.2. Preparation and characterization of CAF-targeted optogenetic system OBA/pHSP-LL37

The human antimicrobial peptide LL37 has been successfully applied in human clinical studies due to its direct killing of pathogens without inducing drug resistance. However, systematically administrated LL37 has poor physicochemical stability and a high risk of disrupting the balance of the systemic microflora. With the development of optogenetic engineering, locally expressing LL37 in the tumor is an emerging and safe method for depleting intratumoral pathogens. Given that CAF has high proportion and preferentially located near blood vessels in BC (Fig. 1A), CAF was listed as the potential candidate for LL37 production. Subsequently, we designed an optogenetic system Au/pHSP-GFP, by loading a green fluorescent protein (GFP) plasmid on a cationic polymer-coated gold nanorod (Au with a good photothermal conversion), to further evaluate the potential of CAF as a cell "factory". After 24 h of intravenous injection of Au/pHSP-GFP (laser for 10 min, 808 W/cm^2), the overall GFP-positive rate of tumor tissue remarkably increased (Fig. 1B and Supporting Information Fig. S2). Among the GFP-positive cells, the average percentage of intratumoral representative cell types was 14.5% (tumor cells), 45.4% (CAFs) and 13.5% (Myeloid

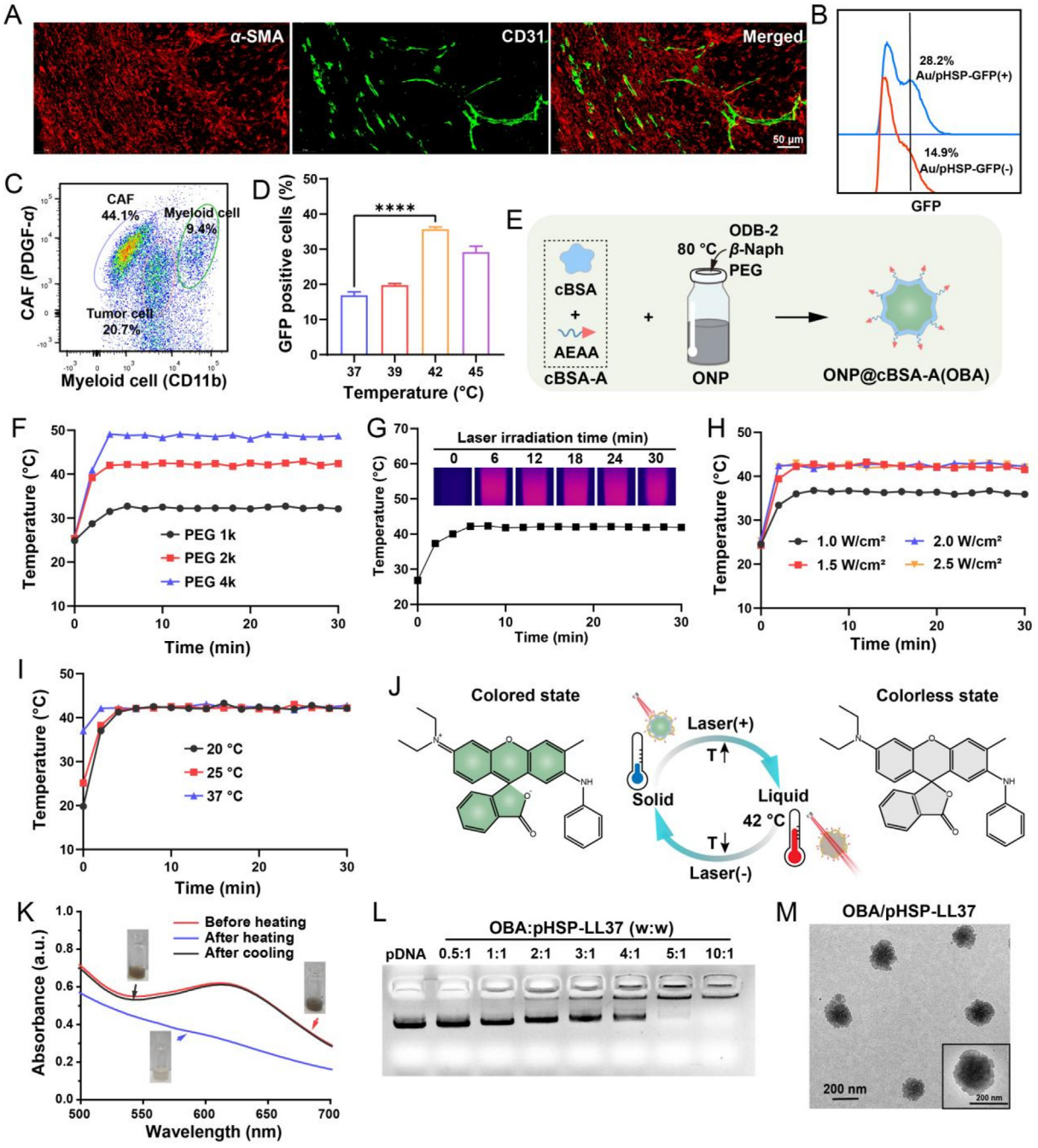

Figure 1 Preparation and characterization of OBA/pHSP-LL37. (A) IF images of α-SMA (red for fibroblasts) and CD31 (green for blood vessels) in 4T1 tumor tissue (BALB/c mice). Scale bar = 50 μm. (B) Representative flow cytometric analysis of GFP-positive cells in 4T1 tumor tissue (BALB/c mice) after treatment with Au/pHSP-GFP *via* intravenous injection. (C) Representative flow cytometric analysis of GFP-positive cells in each population. (D) Quantification of GFP-positive cells after transfection with Au/pHSP-GFP at different temperatures, $n = 3$. One-way ANOVA with Bonferroni's post-test was performed, $^{***}P < 0.001$ and $^{****}P < 0.0001$. Data are represented as mean ± SD. (E) Preparation process of OBA. (F) Heating curves of OBA prepared by PEG with different molecular weights. (G) Thermal infrared images and heating curves of OBA. (H) Heating curves of OBA at different power densities. (I) Heating curves of OBA at different initial temperatures of OBA solution. (J) Schematic illustration of the thermochromic mechanism. (K) UV absorption spectra of OBA before and after laser irradiation. (L) The pHSP-LL37 condensation ability of OBA was determined by agarose gel retardation assay. (M) TEM images of OBA/pHSP-LL37. Scale bar = 200 nm.

cells) (Fig. 1C, Supporting Information Figs. S3 and S4), respectively. These results suggested that CAF is an excellent "factory" for LL37 production in BC.

To maximize the efficiency of the polypeptide expression, we first examined the effects of different temperatures on GFP expression (the cells were treated with a thermostatically heated plate in this study). The results showed that the GFP expression was temperature-dependent and the fluorescence intensity gradually increased when the temperature rose from 37 °C to 42 °C, reaching the highest at 42 °C (Fig. 1D and Supporting Information

Fig. S5). However, GFP fluorescence diminished when the temperature increased to 45 °C (>43 °C, threshold temperature of apoptosis[34]), which may be related to the reduction of CAF activity by hyperthermia (Supporting Information Fig. S6). In conclusion, the results indicated that 42 °C is the optimal temperature for activation of the HSP70 promoter, which is consistent with data mining based on the current literature. However, Au solution increased over 60 °C in about 6 min under laser irradiation (Supporting Information Fig. S7), which severely affected the activity of the transfected cells. Therefore, we urgently need a gene expression vector that can be precisely temperature-controlled.

ONP, consisting of ODB-2 (as a dye), Naph (as a colour developer) and PEG (as a solvent), allow precise control of the melting point temperature by adjusting the molecular weight of the PEG. We tried to construct a thermostatic optogenetic system OBA with ONP as the core and BSA modifying AEAA (a potent ligand for targeting sigma receptor) as the shell (Fig. 1E). We evaluated the successful synthesis of ONP by DSC (Supporting Information Fig. S8). And DLS and FT-IR spectra indicated the successful synthesis of cBSA-A (Supporting Information Figs. S9 and S10). Subsequently, the formed OBA with PEG of different molecular weights (PEG1k, PEG2k, and PEG4k) was characterized. As shown in Fig. 1F, the phase transition temperature of OBA increased with the molecular weight of PEG. The phase transition temperature of OBA is about 42 °C when the molecular weight of PEG is 2k. Therefore, PEG2k was selected as the composition of the final formulation. The precise temperature-control potential of OBA was investigated using an infrared camera. As shown in Fig. 1G, the temperature of the OBA solution increased rapidly from room temperature to 42 °C within 2 min and could be maintained at 42 °C during laser irradiation. We further evaluated the thermostatic properties of OBA by varying the power density of the laser irradiation (Fig. 1H), the concentration of OBA (Supporting Information Fig. S11) and the initial temperature of OBA solution (Fig. 1I). The results all showed that the changes of experimental parameters did not affect the phase transition temperature of OBA. In addition, OBA exhibited excellent photothermal stability after five cycles of laser on and off heating process (Supporting Information Fig. S12).

The principle of precise temperature control: below the melting point of the nanosystem, the phenolic hydroxyl group of the developer interacts with the carboxylate of leuco dye, causing the opening of leuco dye lactone ring, at which point the nanomaterial has colour and can convert the absorbed light into heat under laser irradiation. When the temperature rises to the melting point of the OBA, the solid-state switches to the liquid-state, the lactone ring of leuco dye closes, and the colour changes to colourless, which allows the OBA to stop absorbing light and maintain at a predetermined temperature (Fig. 1J). We observed and recorded the colour changes. Meanwhile, we examined the absorbance of OBA before and after laser irradiation by a UV spectrophotometer. The results displayed that OBA gradually turned from black to colourless during laser irradiation, accompanied with the disappearance of absorption at 620 nm. And the original colour of OBA was recovered after being cooled down to room temperature, together with the restoration of UV−Vis absorption (Fig. 1K). These results indicated the excellent reversible thermochromism of the OBA.

Finally, OBA is loaded with functional plasmids by electrostatic interactions to form an optogenetic system (OBA/pHSP-LL37). Agarose gel retardation assay showed a strong ability of OBA to inhibit the migration of pHSP-LL37 at a low weight ratio (OBA:pHSP-LL37) of 5:1 (Fig. 1L), and OBA could protect pHSP-LL37 from degradation by DNase I when *w/w* (OBA:pHSP-LL37) $\geq$ 5:1 (Supporting Information Fig. S13). DLS results showed that OBA surface potential reduced from +24.5 to +12.2 mV after loading pHSP-LL37 (Fig. S9), indicating that the plasmid was successfully loaded on OBA. CLSM co-localization assay further confirmed the successful preparation of OBA/pDNA (Supporting Information Fig. S14). The particle size of OBA/pHSP-LL37 was approximately 230 nm (Fig. 1M). And the potential, particle size and shape of OBA/pHSP-LL37 in PBS did not change significantly within one week (Supporting Information Fig. S15A−S15C). Furthermore, alterations in the morphology of OBA/pHSP-LL37 were observed at varying laser irradiation times, with minimal change noted for 10 and 30 min (Supporting Information Fig. S16). This indicated that the OBA/pHSP-LL37 has excellent stability.

3.3. *Photothermal-induced the expression of LL37 by OBA/pHSP-LL37*

Cell viability is an important condition for gene transfection, so we first examined the biocompatibility of the OBA/pHSP-LL37 at cellular level. As shown in Supporting Information Figs. S17−S19, CCK8, Hemolysis assay, Taipan blue staining and intracellular ATP measurement assay confirmed that OBA/pHSP-LL37 has great potential for safely engineering cells. Subsequently, cellular uptake of OBA/pDNA was examined in CAF by CLSM. As shown in Supporting Information Fig. S20, OBA/pDNA displayed higher cellular internalization compared to free pDNA and OB/pDNA, indicating that AEAA improved the cellular uptake efficiency of OBA/pDNA. Correspondingly, we observed the lysosomal escape ability of OBA/pDNA by CLSM (Supporting Information Fig. S21). Most of the internalized red-labeled OBA/pDNA was highly co-localized with green-labeled lysosomal after 1 and 3 h incubation, which appeared as yellow dots. At 6 h post-transfection, the yellow dots disappeared and the red fluorescence became more scattered, confirming the endosomal escape ability of OBA/pDNA. In addition, GFP gene was encoded into the plasmid to investigate the optimal experimental condition of OBA/pHSP-LL37 (Supporting Information Fig. S22). Based on the results of flow cytometry (Fig. 2A and B, Supporting Information Fig. S23A and S24A) and CLSM (Fig. S23B and S24B), we selected 30 min as the optimized irradiation time and analyzed the protein expression at 24 h after transfection in the subsequent experiments.

On the basis of above, LL37 expression was estimated in mRNA and protein levels at 24 h after different treatments (laser (+, 30 min) or without (−)). As shown in Fig. 2C, the qPCR results showed that the LL37 mRNA signal exhibited a negligible change in control, OBA(−), and OBA(+) groups without pHSP-LL37. And OBA/pHSP-LL37 (−) group displayed a similar degree of mRNA signal to the control group. In contrast, OBA/pHSP-LL37 (+) induced a much higher degree of LL37 mRNA signal. The expression of corresponding protein was characterized by ELISA, which displayed similar trends in terms of the generation of LL37 protein (Fig. 2D). The above results indicated the excellent ability of OBA driving LL37 expression under laser irradiation (Fig. 2E).

3.4. *OBA/pHSP-LL37 possesses superior antibacterial activity*

Next, we evaluated the antibacterial activity of OBA/pHSP-LL37 *in vitro*. *F.n* was co-incubated with CAF supernatants from different treatments. The growth curves of *F.n* confirmed that OBA/pHSP-LL37(+) completely inhibited *F.n* proliferation

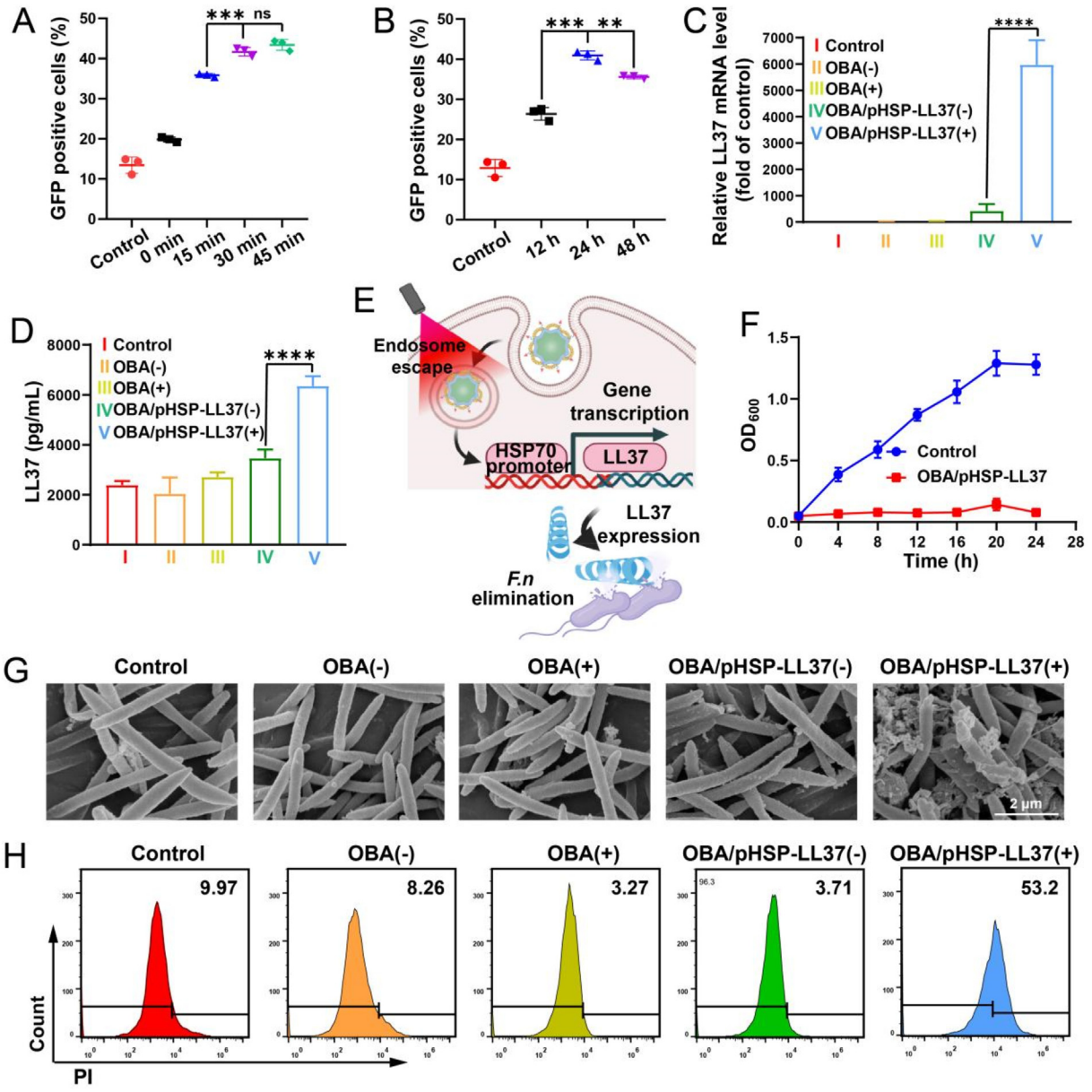

Figure 2 OBA/pHSP-LL37 possesses superior antibacterial activity *in vitro*. (A) Expression of GFP in CAF after transfected with OBA/pHSP-LL37-GFP under different laser irradiation time. (B) Expression of GFP in CAF after transfected with OBA/pHSP-LL37-GFP at different time. (C) LL37 mRNA expression was quantified by qRT−PCR at 12 h after transfection (laser (+) or without laser (−)), $n = 3$. (D) Concentration of LL37 in culture supernatant was analyzed by ELISA, $n = 3$. (E) Schematic illustration of an optogenetic system driving CAF to produce LL37 for depleting *F.n*. (F) Growth curves of *F.n* after different treatments, $n = 6$. (G) SEM images of *F.n* after different treatments. Scale bar = 2 μm. (H) Flow cytometric analysis of *F.n* death after different treatments. One-way ANOVA with Bonferroni's post-test was performed in (B, C, D and E), $^{*}P < 0.05$, $^{**}P < 0.01$, $^{***}P < 0.001$ and $^{****}P < 0.0001$. ns, not significant. All data are represented as mean ± SD.

(Fig. 2F). For a more detailed and intuitive evaluation, *F.n* was observed by SEM after different treatments for 8 h. SEM images showed that *F.n* in control, OBA(−), OBA(+), and OBA/pHSP-LL37(−) groups displayed a smooth surface and was fusiform at both ends. In contrast, *F.n* was clumped and adherent, and the integrity of *F.n* was disrupted following treatment with OBA/pHSP-LL37(+) (Fig. 2G). Further, a large number of *F.n* deaths were also detected by CLSM and flow cytometry in OBA/pHSP-LL37(+) group (Fig. 2H, Supporting Information Figs. S25 and S26). Moreover, LL37 was employed as a positive control group to further verify that OBA/pHSP-LL37(+), similar to LL37, could effectively disrupt the structure of *F.n* (Supporting Information Fig. S27). Together, the above results clearly demonstrated that OBA/pHSP-LL37 could effectively kill *F.n* under laser irradiation.

3.5. *OBA/pHSP-LL37-mediated mild heat normalizes CAFs*

In the preliminary experiments, we found that the morphology of OBA and OBA/pHSP-LL37-treated CAF changed from the previous stellate shape to a long shuttle shape under laser irradiation (Fig. 3A). Given the important role of CAF in metastasis[35-36] and the correlation between CAF morphology and phenotype[37], we

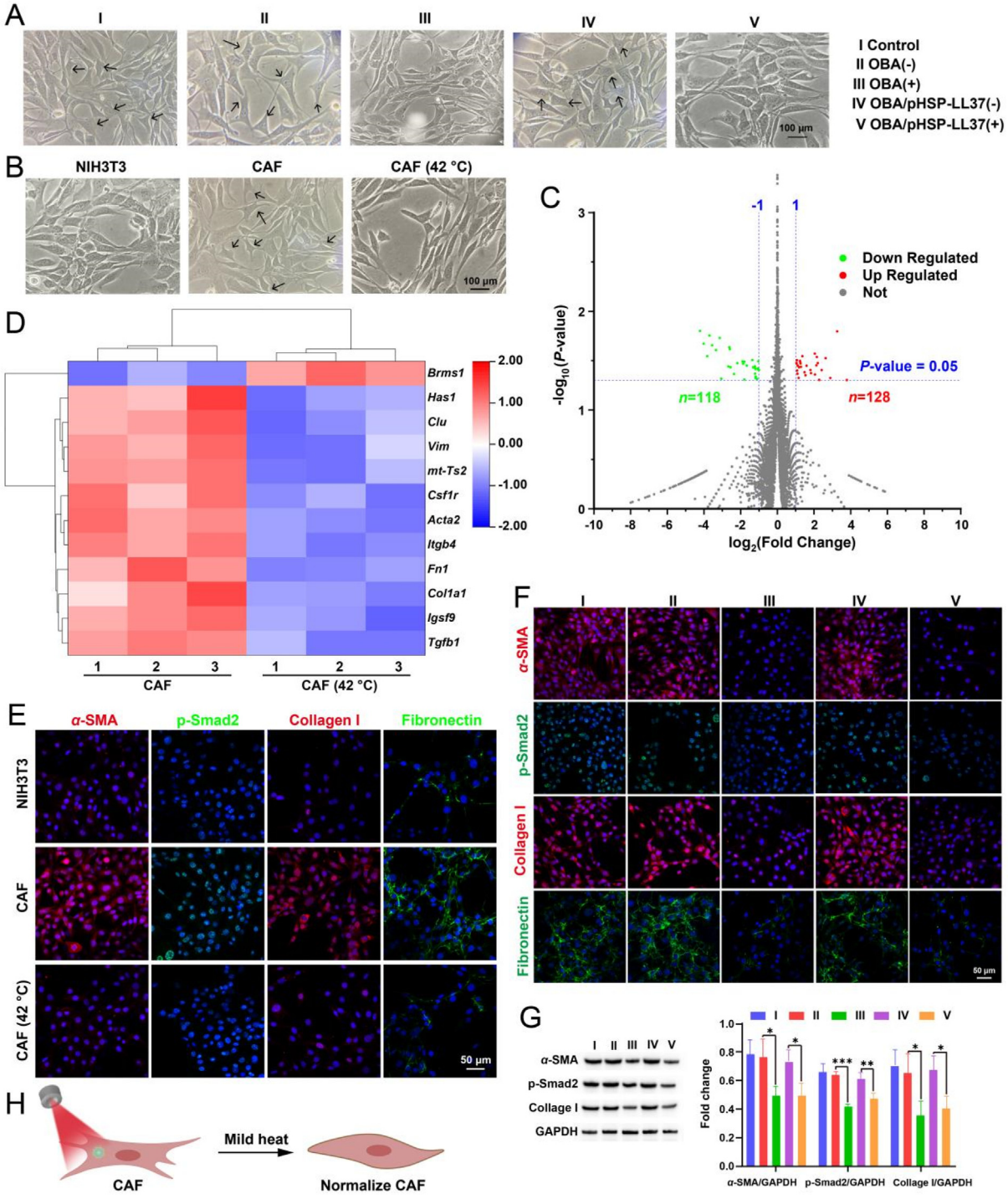

Figure 3 OBA/pHSP-LL37-mediated mild heat reverses CAF phenotype. (A) Morphological changes of CAF after treatment with different preparations (laser (+) or without laser (−)). Scale bar = 100 μm. (B) Morphological changes of NIH3T3, CAF, and CAF treated with thermostatic heating plate. Scale bar = 100 μm. (C) Volcano plot of differentially expressed genes between CAF and CAF (42 °C) groups. Set *P* adj <0.05, $n = 3$. (D) Heat map of differentially expressed genes associated with CAF phenotype ($n = 3$). Red and blue colors represent upregulated or downregulated genes, respectively. (E) IF staining of α-SMA, p-Smad2, collagen I, and fibronectin in CAFs after heating with a thermostatic heating plate. Scale bar = 50 μm. (F) IF staining of α-SMA, p-Smad2, collagen I, and fibronectin in CAFs after different treatments. Scale bar = 50 μm. (G) Western blot analyses of α-SMA, p-Smad2, and collagen I ($n = 3$). Data are represented as mean ± SD. One-way ANOVA with Bonferroni's post-test was performed. (H) Schematic diagram of the mild photothermal-mediated reversal of the CAF phenotype.

examined the effect of heat on CAF. To exclude the effect of the preparation, the cells were treated with a thermostatically heated plate in this study. Untreated NIH3T3 was used as a control. As shown in Fig. 3B, CAF has more cytoplasmic protrusions, spindle-shaped, and has indented nuclei and branching cytoplasm. Unexpectedly, CAF became narrow and elongated, cytosolic protrusions disappeared, and CAF evolved toward an NIH3T3-like cell morphology after treatment with thermostatic plate heating. We speculate that this may be related to the phenotypic alteration.

Next, we further explored the potential molecular mechanisms of heat in CAF regulation by transcriptional analyses. A total of 246 differentially expressed gene profiles were detected. Among these genes, 128 genes were up-regulated and 118 genes were down-regulated (Fig. 3C). The heat map identified 12 representative differentially expressed genes. In particular, genes encoding fibrosis-associated genes (signs of CAF activation) in CAF (including *Tgfb1*, *Col1a1*, *Vim*, *Fn1*, *Acta2*, etc.) were significantly down-regulated after mild heat treatment (Fig. 3D). Subsequently, we again verified the effect of mild heat on CAF state at the protein level by IF. The results showed significant reductions in α-smooth muscle actin (α-SMA, a classic marker for activation of CAF[36]), collagen I and fibronectin (major components of activated CAF secretion[38]) (Fig. 3E). *TGF-β* is the primary factor that drives fibrosis in most[39], the results also showed that *TGF-β1* gene (Fig. 3D) and the downstream *p-Smad2* accumulation of *TGF-β* signaling pathway (Fig. 3E) were significantly down-regulated. Therefore, we speculate that mild heat-normalised CAF should be associated with down-regulation of the autocrine *TGF-β* signaling pathway. This was further corroborated through an examination of the levels of *TGF-β* mRNA (Supporting Information Fig. S28). Further, we examined the effect of OBA with laser irradiation on CAF. The IF images showed that the fluorescence intensity of α-SMA, p-Smad2, collagen I, and fibronectin was decreased after OBA(+) or OBA/pHSP-LL37(+) treatment (Fig. 3F), which was consistent with the Western blot results (Fig. 3G). Together, the mild heat generated by OBA under laser irradiation could efficiently reverse CAF to a quiescent state (Fig. 3H), thereby potentially synergistically inhibiting BC metastasis.

3.6. *In vivo anti-metastasis activity of optogenetic system OBA/pHSP-LL37*

Before examining the anti-metastasis efficacy, the distribution of optogenetic system was evaluated in the orthotopic 4T1 tumor-bearing model. The *in vivo* imaging system showed that OBA/pHSP-LL37-IR783 was effectively enriched at the tumor site and its accumulation at the tumor site was highest after 12 h of intravenous administration (Supporting Information Fig. S29). Next, we confirmed that the temperature of the tumor position in the OBA/pHSP-LL37 group could be maintained at 42 °C under laser irradiation (Supporting Information Fig. S30), indicating the excellent temperature control ability of OBA/pHSP-LL37 and providing support for activating gene expression *in vivo*.

Subsequently, the anti-metastatic activity of OBA/pHSP-LL37(+) was evaluated in spontaneous mouse metastasis models. The timeline of the animal experiments was shown in Fig. 4A. At the end of the treatment, the lungs, one of the main metastatic organs of BC, were dissected and collected to assess the ability of the optogenetic system to prevent metastasis. Obvious metastatic tumor nodules on the surface of the lungs were observed in groups of control, OBA(−), and OBA/pHSP-LL37(−). In contrast, OBA(+), and OBA/pHSP-LL37(+)-treated groups displayed fewer lung metastatic tumor lesions compared to other treatment groups (Fig. 4B and C), and tumor-associated fibroblast activation marker α-SMA was reduced in OBA(+) and OBA/pHSP-LL37(+) groups (Fig. 4D), suggesting that OBA(+)-mediated mild heat can normalize CAFs to prevent BC metastasis. It is worth noting that the number of lung metastasis nodules in the OBA/pHSP-LL37(+) group was significantly lower than that in OBA(+) group, while mice had fewer changes in tumor volume (Supporting Information Fig. S31). FISH results confirmed that OBA/pHSP-LL37(+) effectively eliminated the intratumoral *F.n* (Fig. 4D). In addition, to provide further evidence that LL37 can inhibit tumor metastasis by directly killing *F.n*, an experiment was conducted using immunodeficient mice (BALB/c nude mice) (Supporting Information Fig. S32A). The results showed that the administration of LL37 led to a significant reduction in the number of lung metastatic nodules in the mice (Fig. S32B). And the FISH results corroborated that LL37 was efficacious in eliminating the intratumoral *F.n* (Fig. S32C). The results showed that depletion of *F.n* could prevent BC metastasis.

At the protein level, we further investigated the effect of OBA/pHSP-LL37(+) on metastasis under laser irradiation. We examined tumor sections for representative metastasis-related proteins fibronectin, E-cadherin, and β-catenin. As expected, reduced fibronectin and β-catenin, and enhanced E-cadherin were verified at the protein level in the OBA/pHSP-LL37(+)-treated group (Fig. 4E). The results indicated that OBA/pHSP-LL37(+) could inhibit EMT, thereby suppressing BC metastasis. In addition, masson staining showed a significant reduction in collagen fibre (an important indicator to predict tumor metastasis) in OBA(+) and OBA/pHSP-LL37(+)-treated groups, suggesting that OBA(+) and OBA/pHSP-LL37(+)-mediated mild heat could remodel the tumor ECM to inhibit BC metastasis.

Subsequently, we investigated the effects of OBA/pHSP-LL37 on the intestinal microbiota by 16S rDNA sequencing after more doses. The Alpha Diversity analysis results of gut microbiota showed that no significant difference was found between OBA/pHSP-LL37 and control groups in terms of the Chao1 index (enrichment index) and Shannon index (diversity indices) (Fig. 4F and G). Also, we analyzed the community composition. At the phylum level, the gut flora remained predominantly *Bacteroidetes*, *Firmicutes*, and *Proteobacteria* in each group, suggesting that OBA/pHSP-LL37 has the potential to maintain the balance of the gut microbiota (Fig. 4H). In addition, the Venn diagram showed that the number of OUT shared between the two groups exceeded 70% of the two-sample total OUT, indicating a high similarity between the two groups (Fig. 4I). These results indicated that OBA/pHSP-LL37 did not affect the diversity and abundance of the gut microbiota. In addition, the *in vivo* biosafety of OBA/pHSP-LL37 was investigated by H&E staining of major organ tissues (heart, liver, spleen, and kidney), blood biochemistry and routine examinations after one or more doses. As shown in Supporting Information Fig. S33, compared with untreated mice, no significant histological changes were observed after one or more doses. Similarly, renal function test indexes, liver function test indexes, and blood routine test indexes also suggested that OBA/pHSP-LL37 has high safety (Supporting Information Fig. S34).

3.7. *Optogenetic system OBA/pHSP-LL37-TRAIL suppresses the primary tumor growth*

TRAIL can induce apoptosis in a variety of tumor cells without affecting the activity of normal cells[40], making it an ideal

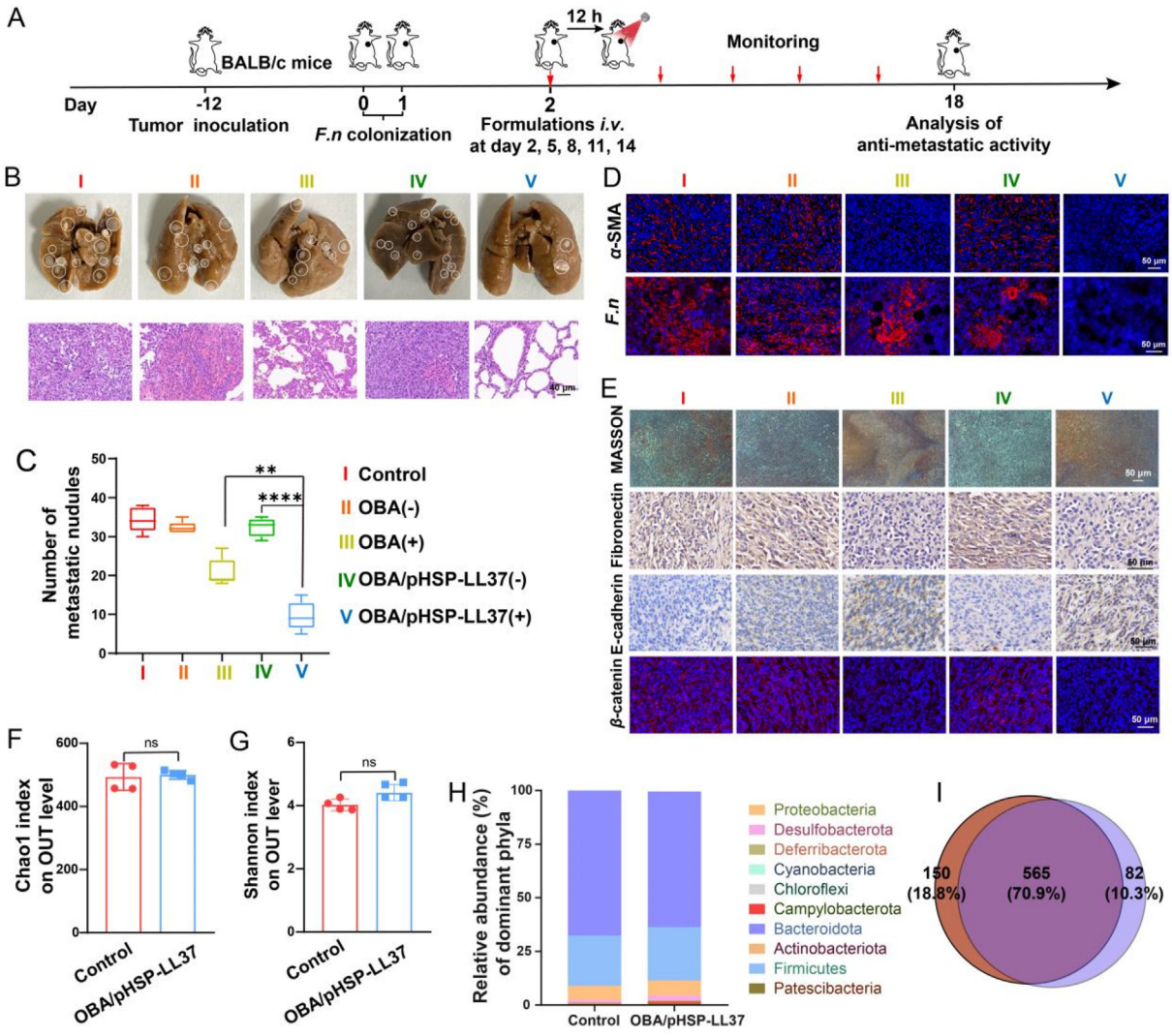

Figure 4 *In vivo* the anti-metastatic tumor activity of optogenetic system OBA/pHSP-LL37. (A) *In vivo* treatment timeline of 4T1 tumor-bearing mice (BALB/c mice). The 4T1 tumor-bearing mice were randomly divided into 5 groups (laser (+) or without laser (−)): control, OBA(−), OBA(+), OBA/pHSP-LL37(−), and OBA/pHSP-LL37(+). The formulation was administered intravenously (i.v.) at two-day intervals for a total of five doses. (B) Photographs and H&E staining of lung metastatic nodules. Scale bar = 40 μm. (C) Quantification of lung nodules after different treatment, $n = 5$. One-way ANOVA with Bonferroni's post-test was performed, $^{*}P < 0.05$, $^{**}P < 0.01$, $^{***}P < 0.001$ and $^{****}P < 0.0001$. (D) IF staining of α-SMA and FISH staining of *F.n* in tumor tissues after various treatments. Scale bar = 50 μm. (E) Masson, IHC and IF staining of tumors after different treatments. Scale bar = 50 μm. Alpha diversity coefficient analysis of gut flora, including (F) Chao1 index and (G) Shannon index, $n = 4$. Two-tailed unpaired t-tests were performed in F and G. ns, not significant. (H) Stacked histograms of relative abundance of bacterial communities at phyla levels, $n = 4$. (I) Venn diagram of generic richness in control and OBA/pHSP-LL37. All data are represented as mean ± SD.

candidate for tumor therapy. Therefore, we constructed a plasmid (pHSP-LL37-TRAIL) encoding the genes of LL37 and TRAIL to safely suppress the primary tumor growth while preventing metastasis (Supporting Information Fig. S35A). TRAIL expression was estimated in mRNA (Fig. S35B) and protein levels (Fig. S35C). Results showed OBA/pHSP-LL37-TRAIL(+) induced the highest level of TRAIL mRNA and protein signal compared to other groups. We also verified the expression of LL37. The qPCR and ELISA results showed no significant difference between OBA/pHSP-LL37(+) and OBA/pHSP-LL37-TRAIL(+) (Fig. S35D and S35E), indicating that the fusion plasmid did not affect the expression of antimicrobial peptides. Next, we examined the ability of secreted TRAIL-induced apoptotic of 4T1 cells by western blotting analysis (Fig. S35F) and flow cytometry (Fig. S35G and S35H). All the results showed that OBA/pHSP-LL37-TRAIL(+) could effectively induce the apoptosis of tumor cells, which provided large support for inhibiting the growth of the primary tumors.

Based on, we investigated the therapeutic efficacy of OBA/pHSP-LL37-TRAIL(+) on large primary tumors (PTX, one of the most widely used chemotherapeutic agents for BC[41], as a control). A tumor-bearing mouse model of *F.n* infection was first established and the timeline of the animal experiments was shown in Fig. 5A. The tumor volumes of the tumor-bearing mice in different treatment groups were measured during drug administration (Fig. 5B). And tumors from different groups were collected

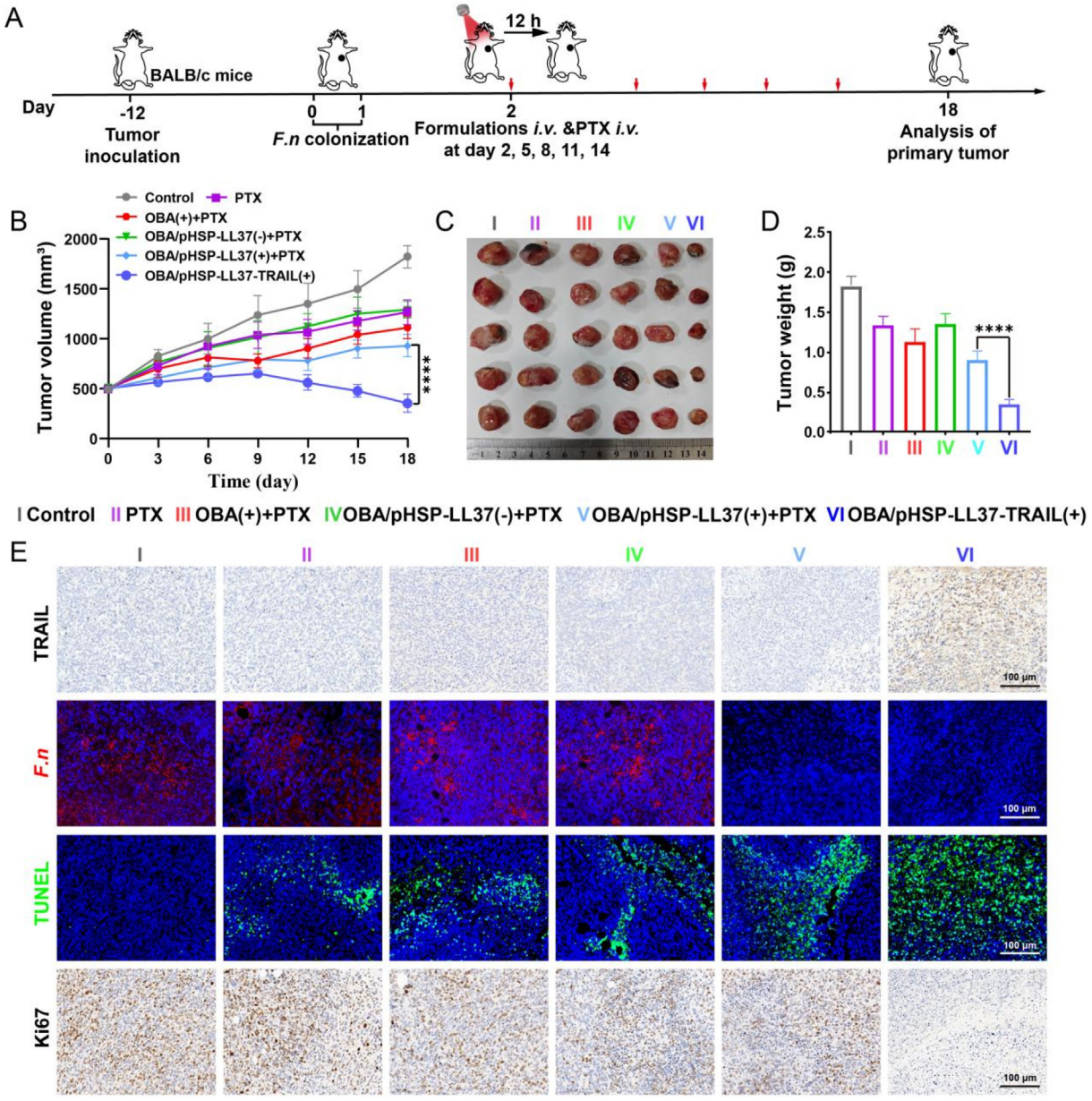

Figure 5 Optogenetic system OBA/pHSP-LL37-TRAIL suppresses the primary tumor growth. (A) *In vivo* treatment timeline of 4T1 tumor-bearing mice (BALB/c mice). The 4T1 tumor-bearing mice were randomly divided into 6 groups (laser (+) or without laser (−)): Control, PTX, OBA(+) + PTX, OBA/pHSP-LL37(−) + PTX, OBA/pHSP-LL37(+) + PTX, and OBA/pHSP-LL37-TRAIL(+). The formulation was administered i.v. at two-day intervals for a total of five doses. After formulation injection, PTX was administered by i.v. injection. (B) Tumor growth curves of 4T1 tumor-bearing mice after different treatments. (C) Photographs and (D) weight of the excised tumors after various treatments. (E) IF, FISH, IHC, and TUNEL staining of the tumors were performed after various treatments. Scale bar = 100 μm. One-way ANOVA with Tukey's post-test was performed in B and D, ****$P < 0.0001$. Data are represented as mean ± SD.

to evaluate the therapeutic efficacy on Day 18 (Fig. 5C and D). As expected, OBA/pHSP-LL37-TRAIL(+) could effectively inhibit the growth of primary tumors, and the tumor volume was approximately 5.1-fold lower than that of control group. Importantly, OBA/pHSP-LL37-TRAIL(+) was more potent in delaying tumor growth (80% inhibition rate) than that treated with OBA/pHSP-LL37(+) + PTX (49% inhibition rate), and body weight changes and blood analysis of mice demonstrated that OBA/pHSP-LL37-TRAIL held the higher safety than OBA/pHSP-LL37(+) + PTX and PTX (Supporting Information Figs. S36 and S37), which should be related to the *in situ* production of TRAIL. Furthermore, the median survival of mice in the OBA/pHSP-LL37(+) + PTX group was approximately 28 days longer than that of the control group (Supporting Information Fig. S38). To further evaluate the therapeutic efficacy of OBA/pHSP-LL37-TRAIL(+), the harvested tumors were sectioned for IHC, TUNEL, and FISH staining. As shown in Fig. 5E, the expression of TRAIL was significantly increased in the OBA/pHSP-LL37-TRAIL(+) group. Obviously, OBA/pHSP-LL37-TRAIL(+) group showed a relatively good anti-proliferative effect on the

tumor according to the Ki-67 analysis. Also, remarkable apoptosis was observed in OBA/pHSP-LL37-TRAIL(+) group. These results indicated the superior antitumor activity of OBA/pHSP-LL37-TRAIL(+). In addition, H&E staining images showed OBA/pHSP-LL37-TRAIL(+) group depleting intratumoral *F.n* also displayed excellent anti-metastasis ability (Supporting Information Fig. S39). Taken together, these results indicated that OBA/pHSP-LL37-TRAIL(+) has the potential to inhibit both primary tumor and metastasis.

4. Conclusions

MBC is a major cause of death in women worldwide, yet the exact mechanisms underlying BC metastasis are poorly understood. With the development of metagenomics sequencing, the intimate relationship between bacteria and BC has been gradually recognized in depth. Especially, the represented pathogenic bacteria-*F.n* increased in abundance in higher stage BC, and has been confirmed to be one of the high-risk factors for promoting BC metastasis. Herein, we constructed a *F.n*-breast tumor symbiont model and revealed that intratumoral *F.n* induced BC aggressiveness by activating the EMT-associated signaling pathway by transcriptome analysis. Thus, depletion of intratumoral *F.n* may provide a new way to prevent BC metastasis.

Considering the important role of balance of the systemic microflora, we reported an optogenetic system to drive CAF *in situ* to produce human antibacterial peptide LL37, with the characteristics of biosafety and freely intercellular trafficking, to deplete intratumoral *F.n* while without affecting the gut microbiota. In addition, the ONP of optogenetic system has excellent reversible thermochromism to allow optogenetic system being maintained at 42 °C under laser irradiation, which can both efficiently initiate gene expression and avoid damaging transfected cells by hyperthermia. Interestingly, we found that mild heat can normalize CAF during experiment, which will contribute to synergistic inhibition of BC metastasis. Overall, our study provides a new horizon for suppressing BC metastasis and suggests that depleting intratumoral *F.n* may have clinical potential to improve the prognosis of breast cancer patients.

Acknowledgments

This work was supported by the National Natural Science Foundation of China (82172762, 21904119, and 82073395); Science and technology innovation talents support project of Henan Province (23HASTIT041), Henan Science Fund for Outstanding Young Scholars (232300421051, China). Authors thank Modern Analysis and Computing Center of Zhengzhou University for technical assistance.

Author contributions

Shizhen Geng: Writing − original draft, Methodology, Conceptualization. Tingting Xiang: Writing − original draft, Methodology, Conceptualization. Yaru Shi: Methodology. Mengnian Cao: Writing − review & editing, Methodology. Danyu Wang: Writing − review & editing, Methodology. Jing Wang: Methodology. Xinling Li: Methodology. Haiwei Song: Writing − original draft, Conceptualization. Zhenzhong Zhang: Supervision, Formal analysis. Jinjin Shi: Supervision. Junjie Liu: Writing − original draft, Funding acquisition, Conceptualization. Airong Li: Supervision, Conceptualization. Ke Sun: Supervision, Resources, Conceptualization.

Conflicts of interest

The authors have no conflicts of interest to declare.

Appendix A. Supporting information

Supporting information to this article can be found online at https://doi.org/10.1016/j.apsb.2025.01.002.

References

1. Jiang Z, Ju Y, Ali A, Chung PED, Skowron P, Wang DY, et al. Distinct shared and compartment-enriched oncogenic networks drive primary *versus* metastatic breast cancer. *Nat Commun* 2023;**14**:4313.
2. Gilam A, Conde J, Weissglas-Volkov D, Oliva N, Friedman E, Artzi N, et al. Local microRNA delivery targets Palladin and prevents metastatic breast cancer. *Nat Commun* 2016;**7**:12868.
3. Palange AL, Mascolo DD, Ferreira M, Gawne PJ, Spanò R, Felici A, et al. Boosting the potential of chemotherapy in advanced breast cancer lung metastasis *via* micro-combinatorial hydrogel particles. *Adv Sci* 2023;**10**:2205223.
4. Wang X, Chen Q, Zhu Y, Wang K, Chang Y, Wu X, et al. Destroying pathogen-tumor symbionts synergizing with catalytic therapy of colorectal cancer by biomimetic protein-supported single-atom nanozyme. *Sig Transduct Target Ther* 2023;**8**:277.
5. Nejman D, Livyatan I, Fuks G, Gavert N, Zwang Y, Geller LT, et al. The human tumor microbiome is composed of tumor type-specific intracellular bacteria. *Science* 2020;**368**:973−80.
6. Park EM, Chelvanambi M, Bhutiani N, Kroemer G, Zitvogel L, Wargo JA. Targeting the gut and tumor microbiota in cancer. *Nat Med* 2022;**28**:690−703.
7. Queen J, Shaikh F, Sears CL. Understanding the mechanisms and translational implications of the microbiome for cancer therapy innovation. *Nat Cancer* 2023;**4**:1083−94.
8. Yu ZK, Xie RL, You R, Liu YP, Chen XY, Chen MY, et al. The role of the bacterial microbiome in the treatment of cancer. *BMC Cancer* 2021;**21**:934.
9. Ma T, Tang Y, Wang T, Yang Y, Zhang Y, Wang R, et al. Chronic pulmonary bacterial infection facilitates breast cancer lung metastasis by recruiting tumor-promoting MHCIIhi neutrophils. *Sig Transduct Target Ther* 2023;**8**:296.
10. Nejman D, Livyatan I, Fuks G, Gavert N, Zwang Y, Geller LT, et al. The human tumor microbiome is composed of tumor type−specific intracellular bacteria. *Science* 2020;**368**:973−80.
11. Fu A, Yao B, Dong T, Chen Y, Yao J, Liu Y, et al. Tumor-resident intracellular microbiota promotes metastatic colonization in breast cancer. *Cell* 2022;**185**:1356−72.
12. Kovács T, Mikó E, Ujlaki G, Yousef H, Csontos V, Uray K, et al. The involvement of oncobiosis and bacterial metabolite signaling in metastasis formation in breast cancer. *Cancer Metastasis Rev* 2021;**40**:1223−49.
13. Mao AW, Barck H, Young J, Paley A, Mao JH, Chang H. Identification of a novel cancer microbiome signature for predicting prognosis of human breast cancer patients. *Clin Transl Oncol* 2022;**24**:597−604.
14. Parhi L, Alon-Maimon T, Sol A, Nejman D, Shhadeh A, Fainsod-Levi T, et al. Breast cancer colonization by Fusobacterium nucleatum accelerates tumor growth and metastatic progression. *Nat Commun* 2020;**11**:3259.
15. Wang S, Li J, Chen M, Ren L, Feng W, Xu L, et al. Palladium nanoplates scotch breast cancer lung metastasis by constraining epithelial-mesenchymal transition. *Natl Sci Rev* 2021;**8**:nwaa226.
16. Lambert AW, Pattabiraman DR, Weinberg RA. Emerging biological principles of metastasis. *Cell* 2017;**168**:670−91.

17. Wang C, Hong T, Cui P, Wang J, Xia J. Antimicrobial peptides towards clinical application: delivery and formulation. *Adv Drug Deliv Rev* 2021;**175**:113818.
18. Lázár V, Martins A, Spohn R, Daruka L, Grézal G, Fekete G, et al. Antibiotic-resistant bacteria show widespread collateral sensitivity to antimicrobial peptides. *Nat Microbiol* 2018;**3**:718−31.
19. Watts S, Hänni E, Smith GN, Mahmoudi N, Freire RVM, Lim S, et al. Human antimicrobial peptide inactivation mechanism of enveloped viruses. *J Colloid Interf Sci* 2023;**657**:971−81.
20. Wei X, Zhang L, Yang Y, Hou Y, Xu Y, Wang Z, et al. LL-37 transports immunoreactive cGAMP to activate STING signaling and enhance interferon-mediated host antiviral immunity. *Cell Rep* 2022;**39**:110880.
21. Mhlongo JT, Waddad AY, Albericio F, De La Torre BG. Antimicrobial peptide synergies for fighting infectious diseases. *Adv Sci* 2023;**10**:2300472.
22. Rodríguez AA, Otero-González A, Ghattas M, Ständker L. Discovery, optimization, and clinical application of natural antimicrobial peptides. *Biomedicines* 2021;**9**:1381.
23. Zhang QY, Yan ZB, Meng YM, Hong XY, Shao G, Ma JJ, et al. Antimicrobial peptides: mechanism of action, activity and clinical potential. *Mil Med Res* 2021;**8**:48.
24. Wang C, Liu X, Chen S, Hu F, Sun J, Yuan H. Correction: facile preparation of phospholipid−amorphous calcium carbonate hybrid nanoparticles: toward controllable burst drug release and enhanced tumor penetration. *Chem Commun* 2020;**56**:10768−9.
25. Domhan C, Uhl P, Meinhardt A, Zimmermann S, Kleist C, Lindner T, et al. A novel tool against multiresistant bacterial pathogens: lipopeptide modification of the natural antimicrobial peptide ranalexin for enhanced antimicrobial activity and improved pharmacokinetics. *Int J Antimicrob* 2018;**52**:52−62.
26. Ding J, Lu J, Zhang Q, Xu Y, Song B, Wu Y, et al. Camouflage nanoparticles enable *in situ* bioluminescence-driven optogenetic therapy of retinoblastoma. *ACS Nano* 2023;**17**:7750−64.
27. Chen X, Chen Y, Xin H, Wan T, Ping Y. Near-infrared optogenetic engineering of photothermal nanoCRISPR for programmable genome editing. *Proc Natl Acad Sci U S A* 2020;**117**:2395−405.
28. Nihongaki Y, Kawano F, Nakajima T, Sato M. Photoactivatable CRISPR-Cas9 for optogenetic genome editing. *Nat Biotechnol* 2015;**33**:755−60.
29. Bordeau BM, Yang Y, Balthasar JP. Transient competitive inhibition bypasses the binding site barrier to improve tumor penetration of trastuzumab and enhance T-DM1 efficacy. *Cancer Res* 2021;**81**:4145−54.
30. Yuan S, Mu W, Liu S, Liu M, Xia Z, Liang S, et al. Transforming cancer-associated fibroblast barrier into drug depots to boost chemo-immunotherapy in "Shooting Fish in a Barrel" pattern. *ACS Nano* 2023;**17**:13611−26.
31. Mahmood MQ, Walters EH, Shukla SD, Weston S, Muller HK, Ward C, et al. β-Catenin, twist and snail: transcriptional regulation of EMT in smokers and COPD, and relation to airflow obstruction. *Sci Rep* 2017;**7**:10832.
32. Fang C, Kang Y, E-Cadherin. Context-dependent functions of a quintessential epithelial marker in metastasis. *Cancer Res* 2021;**81**:5800−2.
33. Wang S, Li J, Chen M, Ren L, Feng W, Xu L, et al. Palladium nanoplates scotch breast cancer lung metastasis by constraining epithelial-mesenchymal transition. *Natl Sci Rev* 2021;**8**:nwaa226.
34. Lyu Y, Cui D, Sun H, Miao Y, Duan H, Pu K. Dendronized semiconducting polymer as photothermal nanocarrier for remote activation of gene expression. *Angew Chem Int Ed* 2017;**56**:9155−9.
35. Liu H, Wang J, Wang M, Wang Y, Shi S, Hu X, et al. Biomimetic nanomedicine coupled with neoadjuvant chemotherapy to suppress breast cancer metastasis *via* tumor microenvironment remodeling. *Adv Funct Mater* 2021;**31**:2100262.
36. Chen X, Song E. Turning foes to friends: targeting cancer-associated fibroblasts. *Nat Rev Drug Discov* 2019;**18**:99−115.
37. Shiga K, Hara M, Nagasaki T, Sato T, Takahashi H, Takeyama H. Cancer-associated fibroblasts: their characteristics and their roles in tumor growth. *Cancers* 2015;**7**:2443−58.
38. Zhang Y, Zhou J, Chen X, Li Z, Gu L, Pan D, et al. Modulating tumor-stromal crosstalk *via* a redox-responsive nanomedicine for combination tumor therapy. *J Control Release* 2023;**356**:525−41.
39. Meng X, Nikolic-Paterson DJ, Lan HY. *TGF-β*: the master regulator of fibrosis. *Nat Rev Nephrol* 2016;**12**:325−38.
40. Miao L, Liu Q, Lin CM, Luo C, Wang Y, Liu L, et al. Targeting tumor-associated fibroblasts for therapeutic delivery in desmoplastic tumors. *Cancer Res* 2017;**77**:719−31.
41. Sofias AM, Dunne M, Storm G, Allen C. The battle of "nano" paclitaxel. *Adv Drug Deliv Rev* 2017;**122**:20−30.